Talanta 81 (2010) 1513–1521

Contents lists available at ScienceDirect

Talanta

journal homepage: www.elsevier.com/locate/talanta

Nanostructure characterization and performance evaluation of perovskite sensor composed of multi-elements

Xubin Pan[b], Sajid Bashir[c], Gang Liang[d], Jingbo Louise Liu[a,*]

[a] Department of Chemistry, Texas A&M University-Kingsville, MSC 161, 700 University Blvd, Kingsville, TX 78363, USA
[b] Department of Environmental Engineering, Texas A&M University-Kingsville, MSC 213, 700 University Blvd, Kingsville, TX 78363, USA
[c] Chemical Biology Research Group (CBRG), The Department of Chemistry, Texas A&M University-Kingsville, MSC 161, 700 University Blvd, Kingsville, TX 78363, USA
[d] The Center of Materials Characterization Facility, Texas A&M University-College Station, 341-P Jack E. Brown Bldg., 3471 TAMU, College Station, TX 77843, USA

ARTICLE INFO

Article history:
Received 26 December 2009
Received in revised form 23 February 2010
Accepted 23 February 2010
Available online 3 March 2010

Keywords:
Li^+-modified $Ca_{0.35}Pb_{0.65}TiO_3$ (LCPT)
Nanosensor
Relative humidity
Nanostructure characterization
Lattice distortion

ABSTRACT

A multi-element perovskite nanoscale film composed of Li^+ cation incorporated into Ca^{2+}-doped $PbTiO_3$ (LCPT) was derived via colloidal chemistry, sol–gel (SG) method followed by heat-treatment. The morphology, chemical composition and structure of the LCPT nanofilms were investigated by advanced instrumentation (microscopy and spectroscopy) techniques. The characterization indicates formation of a tetragonal crystalline ceramic after sintering. The humidity sensing performances of LCPT nanofilms with various formulations were evaluated as a function of lattice distortion. The LCPT sensor doped with Li (0.5–0.1 mol%) possessed the distortion of 1.041–1.046 and displayed rapid sensitivity (current changes from 1.5×10^{-3} to 5.2 A), high linearity ($R^2 = 0.997$) in the whole relative humidity range (φ: 8–93% RH) under low frequency of 100 Hz, and excellent long-term stability.

1. Introduction

Accurate measurement of water vapor content (relative humidity) is an important factor in numerous applications [1]. In this regard, it is critical that measurements are accurate, precise and stable, especially for monitoring atmospheric humidity [2]. A number of methods have been developed in the measurement of humidity. These have focused on electrical sensors [3] through measurement of capacitance [4] or interferometer [5]. Recently, the change in gold nanoparticles to protein localized surface plasmon resonance [6] which has the advantage of sensitivity [7]. Deliquescence properties of sodium chloride have also been used to measure humidity which is modeled to increase with decreasing particle diameter [8]. In the aerosolized form the deliquescence can incorporate between one to four monolayers of water adsorbed on the surface [9] yielding higher sensitivity than the bulk surface. Other approaches include use of electrolytes [10], alumina thin films [11], salts [12], organic (bio)polymers [13] or ceramics [14] from which miniature humidity sensors can be are fabricated [15].The advantages of ceramic-based sensors are improved chemical, thermal or mechanical stability [16]. Previous attempts have focused on use of ZrO_2 [17], $ZnCr_2O_4$ [18], $MgAl_2O_4$ [19] and other systems such as α-hematite [20]. The current focus is on the development of a ceramic sensor based on perovskite family using sol gel processes. Perovskite materials are a large family of crystalline or amorphous ceramics which are of practical importance, due to their dielectric, piezoelectric, ferroelectric, and mechanical properties [21]. One key member of this perovskite family is lead titanate ($PbTiO_3$) [22], which have attracted attention, because of its potential application in areas such as: dynamic access memory, electro-optical devices, and sensors and actuators [23]. It has been hypothesized that crystalline structure and close packing are related to applicability. $PbTiO_3$ crystals commonly resort to a face-centered tetragonal structure below the Curie temperature, T_c [24]. When the temperature is lowered towards the Curie point, a well-known first-order phase transition occurs from the prototype cubic to tetragonal phase [25]. The $PbTiO_3$ possesses high tetragonality (defined as the relative ratio of lattice constant of c over a, denoted as $\delta = c/a$) resulting in a large internal stress during the cooling process through the Curie point. These stresses often cause cracking and deformation of the microstructure [1]. A possible method to eliminate this deformation is to modify lead titanate though A-site substitution via doping suitable ions such as calcium ions (Ca^{2+}). Doped materials possess smaller tetragonal distortion leading to a lowering of internal stress. Therefore, modification of $Ca_xPb_{1-x}TiO_3$ films can be accomplished, resulting in relief of microstructure distortion which is related to the amount of the doped Ca^{2+} present [26]. In addi-

* Corresponding author. Tel.: +1 361 593 2919; fax: +1 361 593 3597.
E-mail addresses: panadin@hotmail.com (X. Pan), br9@tamuk.edu (S. Bashir), gliang1972@neo.tamu.edu (G. Liang), kfjll00@tamuk.edu (J.L. Liu).

0039-9140/$ – see front matter © 2010 Elsevier B.V. All rights reserved.
doi:10.1016/j.talanta.2010.02.063

tion, lithium ions (Li^+, due to their high charge density) can also be employed to change the electronic properties of the $Ca_xPb_{1-x}TiO_3$ film, ultimately resulting in enhanced performance of the humidity sensor compared to the sensor without lithium modification [27] due to changes in the dielectric constant. It has been previously observed that doped $PbTiO_3$ nanofilms demonstrate higher piezoelectric and pyroelectric figures of merit than the undoped substance [28].

In order to produce nanoscale materials, there are several approaches developed, such as sol–gel (SG) synthesis, inert gas condensation, mechanical alloying, or high-energy ball milling, plasma synthesis, and electro-deposition [29]. In our study, the cost effective SG technique was employed to fabricate the nanoscale material, especially for the Li-modified $Ca_xPb_{1-x}TiO_3$ nanofilms. This method can offer the significant advantages, such as high purity, chemical homogeneity, controlled particle size, and large surface area [30]. This SG method also allows the preparation of a mixture in an aqueous solution, achieving homogeneity on the molecular scale in the solid product [31]. The SG method followed by solid-state chemistry is becoming an increasingly popular route for the preparation of multi-component metal oxides, such as the $PbTiO_3$-based materials [32]. Increasing attention has recently been focused on SG-formed oxides with highly porous structure, providing very high surface areas, which favors the chemisorptions of the analyte on the surface of the thin films [33]. In this study, our aims were to prepare uniform nanothin films of $PbTiO_3$ by the SG method, which were modified through doping with Ca^{2+} (and/or) Li^+ cations, in order to decrease lattice distortion and increase electrical properties of the final assembled sensor, respectively. The current work focused on nanocharacterization of the film sensor through analytical techniques such as transmission electron microscopy (TEM), atomic force microscopy (AFM) and laser Raman spectroscopy (LRS). TEM was used to evaluate the structure of the final product composed of lithium-modified $Ca_{0.35}Pb_{0.65}TiO_3$ (abbreviated as LCPT) ceramic films, generated using the SG method [34]. Particle size and size distribution can also be determined from which the triple phase boundary (TPB) and surface area can be evaluated. AFM was used to identify the surface topology and height roughness from which pore size and grain boundaries can be determined [35]. LRS was used to measure all longitudinal (LO) optical and transverse optical (TO) modes [36]. The addition of Ca^{2+} and/or Li^+ into the $PbTiO_3$ lattice provides new information on the soft mode behavior of this perovskite material, consequently resulting in the enhanced performance of the sensor.

2. Materials and methods

The construction of the sensor will be presented first followed by fabrication of the sensing element and sensor operability (Section 2.1). Its surface topology and vibrational structure was characterized using state-of-the-art instrumentation (Section 2.2). The sensor performance and humidity sensing mechanism were evaluated and discussed (Section 2.3).

2.1. Materials preparation

All chemicals, solvents, and reagents unless otherwise specified were obtained from VWR International, (West Chester, PA) or Sigma–Aldrich (St. Louis, MO). Double-distilled, filtered ultrapure water was used (Ultraopure™, Barnstead, Dubuque, IA, referred to as distilled water), was used where water-based solvents were necessary and all solvents were reagent or HPLC grade.

SG technique was applied to fabricate the sensor precursor containing multi-elements of lithium (Li), calcium (Ca), lead (Pb), titanium (Ti), and oxygen (O). The starting materials of titanium(IV) n-butoxide ($Ti(OBu)_4$) was dispersed in normal butanol ($C_4H_{10}O$) and high agitation (1000 rpm) was applied for 30 min. Li, Ca and Pb nitrates ($LiNO_3$, $Ca(NO_3)_2{\cdot}4H_2O$, $Pb(NO_3)_2$) were dissolved in distilled water and then simultaneously injected into the Ti-containing solution. The mixture was agitated, for further 30 min until a homogeneous colloidal suspension was formed at ambient temperature and pressure. The LCPT sol-precursor was deposited via spin-coating onto the interdigited electrode which was composed of the aluminum oxide (α-Al_2O_3) coated with gold (Au) and palladium (Pd) alloy (1:1 mass-to-mass ratio). After five coating layers, the base sensing element was heated at various temperatures (from 600 to 1000 °C in air, at a heating rate of 2, 10, or 20 °C/min), and it was noticed that 850 °C was the optimal temperature (in terms of crystallinity and particle size) [37]. The overview of the LCPT sensor was displayed in Fig. 1 (and illustration of sensor design Fig. S1(a) and (b) in supplemental section). It can be seen from Fig. 1 that integration of nanoparticle sensing element into macrosensor yields the high performance of nanosystems, such as high surface area, speed of detection with the robustness and ease of use of a macrodevice.

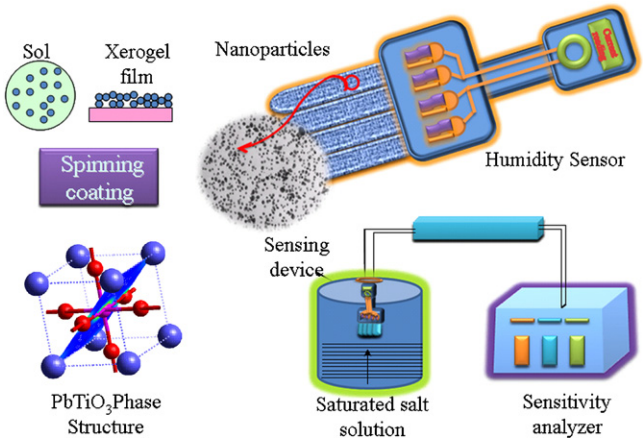

Fig. 1. Overview of sensor construction and detection method.

2.2. Nanostructure characterization

Four advanced instrumentations were employed to study the surface topology of the particles of the sensor elements. A Tecnai F20-G^2 high-resolution transmission electron microscopy (HRTEM) (FEI Company, Hillsboro, Oregon) with electron diffraction (ED) capabilities was employed in this work in order to obtain nanostructured and crystalline phase information about the SG-formed LCPT sensor. Selective area electron diffraction were obtained at a 75 kV accelerating voltage. Atomic-resolved lattice fringe of LCPT materials were characterized at 200 kV and equipped with slow scan cooled CCD (Gatan) camera with the digital micrograph software with resolution of 1 mega pixel. A NanoScope IIIa Atomic Force Microscopy (AFM) (Veeco Instruments Incorporation, Plainview, NY) with taping mode capabilities was employed to obtain the surface topology and height roughness about the SG-formed LCPT sensor. The tapping AFM was conducted with stiff crystal silicon probes. The tap velocity was controlled at approximately 23.5 μm/s and sample line of 256 was used. In order to increase the ratio of signal and noise, slow scan rate of 0.587 Hz was applied. A Spex 1403 Laser Raman Spectroscopy (Renishaw Plc, Edison, NJ) with double monochromator (HeNe laser, operated at 632.8 nm) was employed to determine the lattice vibration frequencies and molecular structure of the LCPT sensor. An argon-ion laser with emission wavelength of 541.5 nm was used in this study. The resolution was 1.0 cm^{-1}. The wavelenth ranged from 800

Table 1
Structural and operational data of Li^+-modified $Ca_{0.35}Pb_{0.65}TiO_3$ humidity nanofilms.

Specifications of the LCPT sensor	
Dimension of the sensor (mm)	$8 \times 10 \times 0.025$
Average particles of LCPT (nm)	22.8
Operating temperature (K)	298
Operating relative humidity (RH%)	8–95
Sensitivity (Order of magnitudes in current)	0.001–1
Supply voltage (V)	4
Previous works cited	
Frequency (Hz)	0.5–10,000
Standard Resistance (()	100
Response time during absorption (s)	7.8
Response time during desorption (s)	9.8
Hysteresis (%)	±2.2
Stability (after 12 months)	±2.8

to 20 cm^{-1} at ambient temperature and pressure. X-ray powder diffraction (XRD) with copper (Cu) diffractometer and visual XRD Jade 7 software (Rigaku Americas Incorporation, Houston, TX) was employed to determine the phase structure and crystalline size. To study the lattice constant and then calculate the microstructure distortion, the slow scanning at 0.05°/min between 30 and 33° was used to obtain high-resolution XRD data.

2.3. Sensor performance evaluation

Adsorption of water vapor onto the absorption surfaces will lead to enhancement of electrical conductivity (or resistance) of metal oxides, from which sensor performance can be tested. Over prolonged usage, the sensor may lose sensitivity due to exposure to other air-borne contaminates in addition to water vapor via both physical and chemical processes between these contaminates and the sensor surface. If the nanostructure is in the powered form, this can lead to signal variation especially over high temperature 'clean cycles', which is not an issue with ceramic film based surfaces. The perovskite family contains up to 0.5–1.0 mol% Li and demonstrates a single-phase solid solution. This single phase is indicative of uniformity and high purity of the sensor and is reflected in the measured tetragonality. The properties of the LCPT are summarized in Table 1. The electrical performance of the sensor under varying relative humidities and various formulations (Table 2) were measured using a GR 1658 RLC Digibridge Impedance Bridge (DIB) w/test adaptors (USA GenRad, Westbury, NY). This DIB equipment was used to measure the resistance or current to determine sensor performance. The operating conditions were controlled at voltage of 4 V, standard resistance 100 kΩ, frequency varying from 0.5 to 10,000 Hz. The relative humidity was created using various saturated aqueous salts solutions.

3. Results and discussion

The integration of nanoscaled particles in a macroscale sensor allows certain advantages, such as increased reactive surface area for sensing, rapid response time which when incorporated into the macro-system, such as humidity sensor, yields the above advantages plus ruggedness, ease of read-out and portability. The bulk of publications discuss concepts or demonstrations of materials and device properties, but few address nano-macro-integration. The key lies in the understanding and manipulating the interfaces between nano-, micro-, and macroscale for both materials and devices to optimize device performance at both levels of design. Significant improvements in materials properties enabled by nanostructure are the focus of optimization of the humidity sensor. An in-depth understanding of the sensor properties was obtained through nanocharacterization (by TEM and AFM, Sections 3.1 and 3.2) for determination of grain boundaries, pore structure, triple phase boundaries and local topology. LRS analysis was used to address the vibrational mode of the modified perovskite-based materials (Section 3.3) to provide the experimental validation necessary for rapid, iterative development of the nanotech-enabled system. XRD analysis (Section 3.4) was carried out to determine the tetragonality of the LCPT nanoparticles of varying formulations (Table 2), from which device sensitivity can be optimized. Lastly, electrochemical properties of the LCPT sensor were evaluated by measurement of current under different relative humidity conditions (Section 3.5).

3.1. Transmission electron microscopy (TEM) analysis of LCPT sensor

The TEM micrograph indicates that the average particle size was approximately 18 nm (Fig. 2a). It was also noticed that the particles were on the whole mono-dispersive (±4 nm) and certain degree of agglomeration occurred upon heat-treatment at high temperature 850 °C. In general, nanoscale particles resulted in a larger surface area and longer phase boundary length than the bulk phase, which favored increased sensitivity and response time (due to increased water chemisorption). Ultrafine particles (<8 nm) were not synthesized, since these are subject to mechanical peeling in the sensor and consequentially were not observed. On the other hand, coarse particle sizes (>30 nm) which contribute to lower surface areas were not synthesized nor observed. From our studies, crystallite sizes ranged from 8 to 30 nm, which resulted in rapid sensitivity (three orders of magnitude in current change, *cf.* Fig. 7a3, Section 3.5) with excellent mechanical strength of the LCPT sensor which is typical of ceramic-based sensors [38].

The indexing of selected area electron diffraction (SAED) pattern from the $PbTiO_3$ single crystal region is shown in Fig. 2b. This indicates that the perovskite LCPT crystalline structure was of high purity since it correlated with the standard based on the Joint

Table 2
The selection of tetragonality of various Li^+-modified $Ca_{0.35}Pb_{0.65}TiO_3$ sensors.

# of samples	Ca dopant (mol%)	Heating rate (°C/min)	Heat-treatment temperature (°C)	Tetragonality
1	30	2	900	1.050
2	30	10	900	1.049
3	30	20	900	1.048
4	30	20	800	1.046
5	30	20	700	1.042
6	35	20	900	1.046
7	35	20	800	1.044
8	35	20	700	1.040
9	50	20	900	1.045
10	50	20	800	1.043
11	50	20	700	1.040

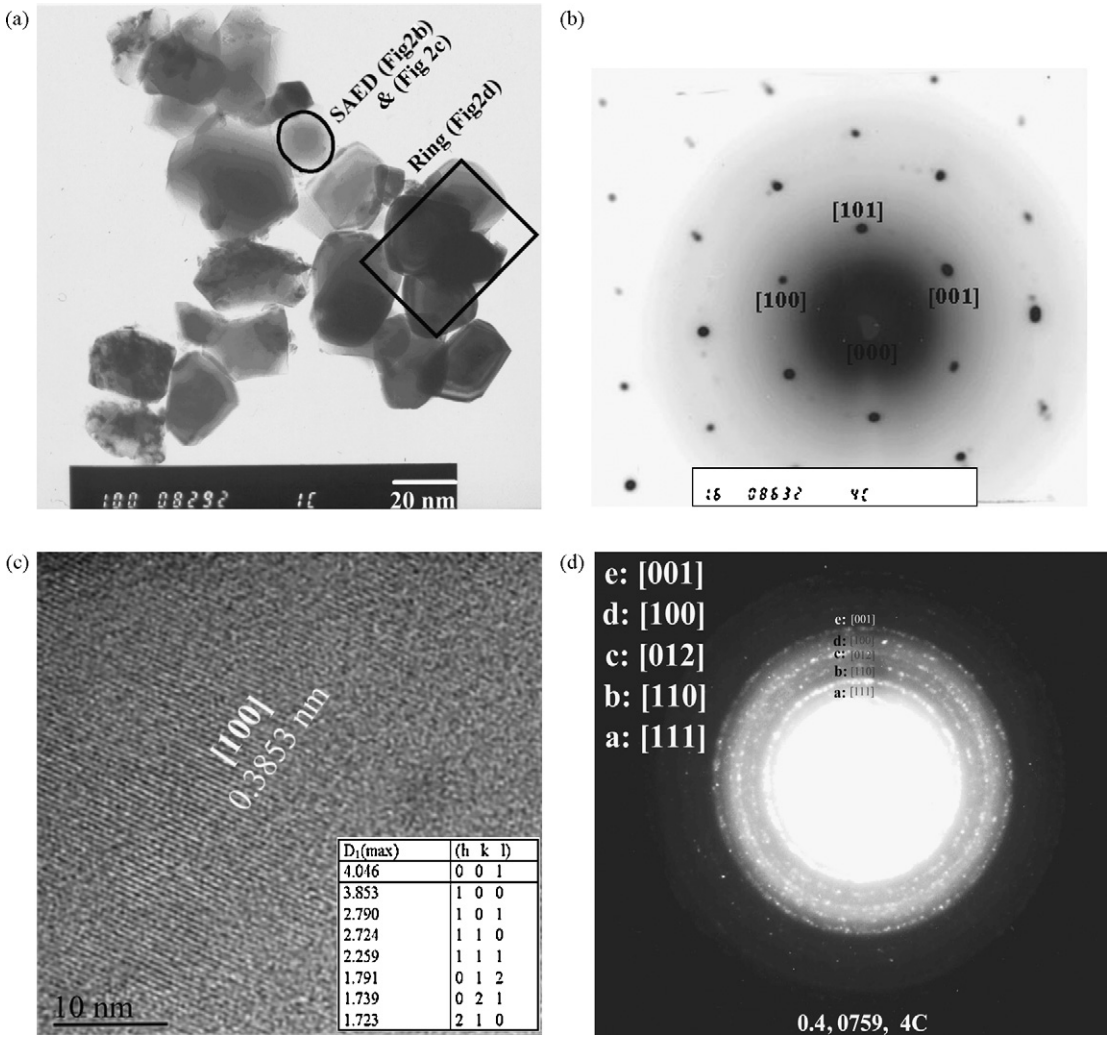

Fig. 2. (a) TEM image of LCPT nanopowders. (b) Selected area electron diffraction (SEAD) of LCPT from single crystal unit. (c) Lattice fringe of LCPT from single crystal unit. (d) Ring patterns of LCPT from polycrystals region.

Committee on Powder Diffraction Standards (PDF 06-452). The identification of the Miller indices demonstrates that a highly crystallized LCPT was obtained. Atomic resolution TEM image (Fig. 2c) for the single crystal unit confirms that the LCPT crystal structure was well defined although few stacking faults were observed. The distance between adjacent fringes was approximately 0.3853 nm identical to the *d*-spacing of the [1 0 0] plane of the standard, $PbTiO_3$. From the analysis of the halo-ring patterns from the polycrystals (Fig. 2d), it was confirmed that well ordered crystallized LCPT was formed because the diameter of the rings corresponded to the *d*-spacing of the tetragonal phase structure. No second phase was detected in our study [39]. Collectively, these studies demonstrate that the nanoparticles were of high purity and crystallinity as confirmed by XRD.

3.2. Atomic force microscopic analysis of LCPT sensor

The surface topology and the height roughness of the LCPT sensor (Fig. 3a) are consistent with the formation of nanoscale films. The films contour was compact and uneven along the *z*-axis and showed the presence of sub-domains formed by polycrystalline particles, with areas averaging approximately 1 μm × 1 μm. These domains provide significant advantage for chemisorptions of water molecules when the sensor was exposed to moisture. From the 2D micrograph (Fig. 3a) (and 3D in Fig. S2 supplemental section) it was noted that uniform films (in the *x*–*y* plane) were formed which were also highly densified. From the micrograph, the grain boundary can also be easily distinguished, which favors chemisorption of the water molecules. Although speculative, it can also be seen from the micrograph and our illustration (Fig. 3b) that water molecules adsorbed on the neck and grain boundary region can be desorbed under standard temperature and pressure due to the increased surface area relative to the bulk powered form. This water adsorption or desorption is reflected in changes of measured current and indicate fast kinetics, an advantage of the nanoscaling. It was also seen that the root mean square (RMS) roughness (or unevenness) of surface was about 54 nm, which indicates that the deposition of the LCPT film was uniform and the film particles were mono-disperse [40]. A physical sensing mechanism for humidity is shown in the schematic (Fig. 3b) based on the AFM micrograph (Fig. 3a). The schematic indicates sites of water adsorption in the LCPT sensor. The nanoparticles adsorb water vapor throughout its well-defined pore structure and condense within the grain surfaces. The condensation of water vapor tends to occur more towards the 'neck' of the grain surfaces, which resemble the bulk itself, from which the measured current can give an estimation of the relative humidity to a high precision. Water adsorption can conceptually be thought of being chemisorbed on the neck through ionic interactions, which results in water dissociation ((i) $H_2O \rightarrow HO^- + H^+$). Lithium substitution leads to creation of an 'oxygen vacancy', ((ii) Ca^{2+} substituted

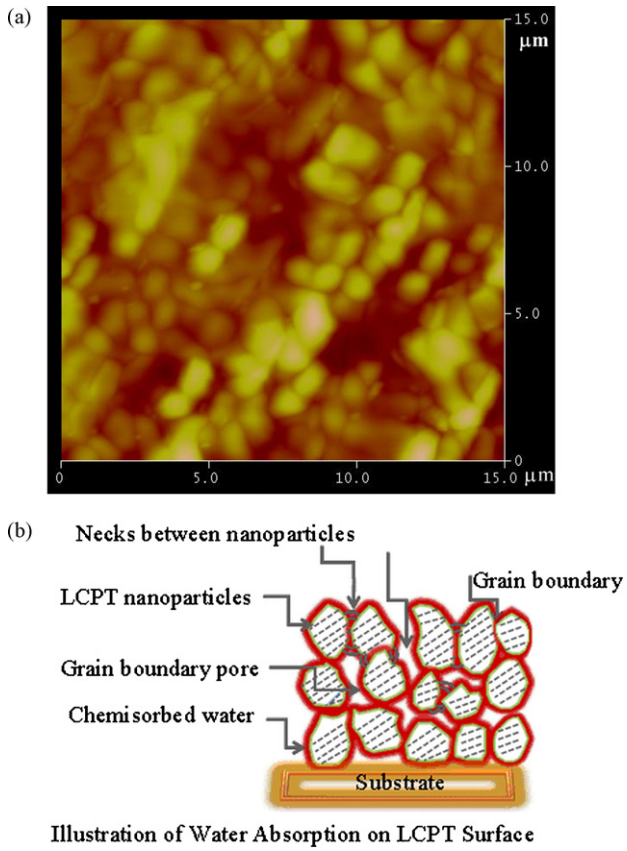

Fig. 3. (a) Two-dimensional AFM topology of LCPT sensor surface. (b) Schematic of LCPT sensor surface correlating to AFM two-dimensional topology.

by Li^+ and oxygen vacancy $\left[V_O^{\bullet\bullet}\right]$ created, (iii) OH^- occupies $\left[V_O^{\bullet\bullet}\right]$ and H^+ interacts with O–Ti, via dipole–dipole intermolecular forces (Section 3.5)). Therefore the charge carriers are between the substituted Li^+ ions and resulting oxygen vacancies in the LCPT and adsorbed water molecules on the neck with the mobile proton (generated in step (i)) migrates across the surface via different sites. As the water content increases, multilayers may be created due to long range interactions of the water molecules with the inner core hydroxyls, at the neck through hydrogen bonding. This may lead to an increase in current (due to increase in proton concentration) when the relative humidity was increased (Section 3.5). The increase in measured current can therefore be assigned to protonic conductance and formation and occupancy of oxygen vacancies by the anionic oxygen from the hydroxyl group. It can be concluded that the film posses large specific surface area and 'good' electrochemical behavior which results in fast reversible kinetics and low hysteresis for humidity sensing.

3.3. Laser Raman spectroscopic analysis of LCPT sensor

Laser Raman Spectroscopic (LRS) study of the sensor depicted that there existed significant differences (Fig. 4a and b between the Raman spectra of LCPT and those of pure $PbTiO_3$ [41]). The five Raman peaks ($2A_1(TO)+2E(TO)+1(B_1+E)$) of LCPT (Fig. 4a), appearing at 75, 125, 190, 273 and 585 cm^{-1} were attributable to the red shift and extension of E(1TO), A_1(1TO), E(2TO), B_1+E and A_1(3TO) vibration soft mode of the perovskite tetragonal phase, respectively. It is commonly agreed that ferroelectric phase of $PbTiO_3$ exhibits a tetragonal symmetry with C_{2v}^1 space group at ambient temperature. Ten optical modes ($3A1(TO)+1A_1(LO)+3E(TO)+2E(LO)+1(B_1+E)$) for the C_{2v} point

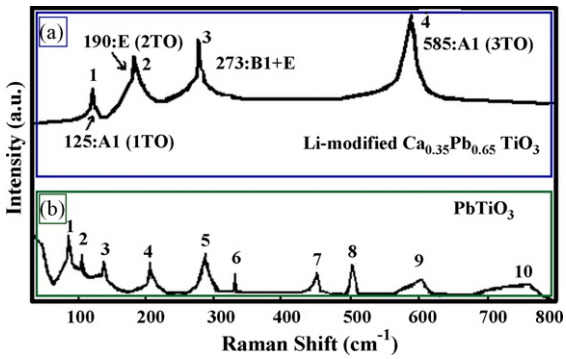

Fig. 4. (a and b) Raman spectra of pure $PbTiO_3$ and Li-modified Ca-doped $PbTiO_3$ LCPT sensor. (a) Spectrum of Li-modified $Ca_{0.35}Ti_{0.65}O_3$; (b) spectrum of $PbTiO_3$.

group were detected and they were assigned to A_1(TO), A_1(LO), B_1+E, E(TO), E(LO), where LO and TO refer to longitudinal and transverse optical modes [42]. It can be seen that the five characteristic LRS bands of $PbTiO_3$ (Fig. 4b) become Raman silent modes due to the higher symmetrical atoms arrangement in LCPT crystal, corresponding to the reduction of tetragonality. The assignments of the Raman bands and their attributions were summarized in Table 3. Briefly, the Raman spectra of the non-modified $PbTiO_3$ were assigned at the following: the 84 cm^{-1} results from E(1TO) optical mode (1), 105 cm^{-1} from E(1LO) mode (2), 145 cm^{-1} from A1(1TO) mode (3), 203 cm^{-1} from E(2TO) mode (4), 289 cm^{-1} from B1 + E mode (5), 332 cm^{-1} from A_1(2TO) mode (6), 447 cm^{-1} from E(2LO) mode (7), 500 cm^{-1} from E(3TO) mode (8), 597 cm^{-1} from A_1(3TO) mode (9) and 757 cm^{-1} from A_1(3LO) mode (10) [43]. These ten measured peaks represent the vibration modes in the tetragonal $PbTiO_3$ with the largest tetragonality. The frequency and intensity in these modes also indicated that unsymmetrical vibration and high dipole–moment of Pb–O and Ti–O bonds which result in the Raman active spectra [44]. On the other hand, when the Ca^{2+} ion ($r=0.099$ nm) replaced Pb^{2+} ion ($r=0.120$ nm) in the A-site of the tetragonal structure, the tetragonality is decreased according to the Ca^{2+} molar percent. With the increase of the mole percent Ca^{2+} content, the tetragonality is further decreased, which means that the phase structure of LCPT tends to be transformed to cubic from tetragonal. When Pb^{2+} cation is completed replaced by Ca^{2+}, the primitive cubic phase will be obtained. In this study, the Li-modified and Ca-doped $PbTiO_3$ with lattice distortion varying from 1.040 to 1.055 is delicately designed to achieve high sensitivity. From our previous study using X-ray powder diffraction [41], the tetragonality of $PbTiO_3$ is 1.064 which is essentially identical to the reported value 1.065 (0.4156/0.3902 nm) [45,46]. When Ca^{2+} dopant varied from 0.15 to 0.35 mol%, the tetragonality was decreased from 1.064 to 1.051 and to 1.040, respectively. Due to the diminished tetragonality, the octahedral structure of the TiO_6 and dodecahedral PbO_{12} become more symmetrical [47]. Therefore the dipole moment of the lattice vibration and polarization are both decreased, which translate to a decrease in the observed Raman activity [48]. Compared with the $PbTiO_3$ face-centered tetragonal structure, the frequency of the LCPT was subject to red shift and the line intensity was decreased [49]. Five bands (Table 3 and Fig. 4a) in LCPT were obtained which resulted from E(1TO), A_1(1TO), E(2TO), B_1+E, and A_1(3TO) optical modes, whereas the remaining become Raman inactive.

The decrease in the vibrational modes from $PbTiO_3$ to LCPT can be attributed to the high symmetry of the LCPT unit cell [30]. According to the "soft mode theory" applied to ferroelectric materials, the spontaneous polarization in the crystal structure can be studied [38,50]. This polarization is highly indicative of the vibrational modes of Raman spectra. The terminology of the "soft mode"

Table 3
LRS spectra assignments of Li^+-modified $Ca_{0.35}Pb_{0.65}TiO_3$ humidity nanofilm.

Spectra peaks (cm^{-1})		Peak mechanism
Undoped $PbTiO_3$	Li-modified $Ca_{0.35}Pb_{0.65}TiO_3$	
84	75	E (1TO)
105	Raman inactive	E (1LO)
145	125	A1 (1TO)
203	190	E (2TO)
289	273	B1 + E
332	Raman inactive	A1 (2TO)
447	Raman inactive	E (2LO)
500	Raman inactive	E (3TO)
597	585	A1 (3TO)
757	Raman inactive	A1 (3LO)

is defined as the recovery coefficient of the vibrational mode is going to be decreased with the temperature decrease or the Ca dopant increase. With the temperature decrease and Ca dopant increase, the frequency of the vibration in the crystal structure is also decreased [30], known as "soft mode". When the frequency of the vibration approaches to zero, the lattice cannot transfer from one phase to another state which indicates a formation of the new phase, known as phase transition [37]. This transition is located in the center of the Brillouin zone. When $PbTiO_3$ is subjected to a decrease in temperature when passing the T_c, the cubic phase is transformed to tetragonal phase. Some vibrational frequencies in the lattice are subject to a decrease and become stationary (unchanged) [51]. Therefore, at these temperatures, the tetragonal phase cannot be transformed to the cubic phase. According to the energy distribution, the optical frequency is related to the Raman active modes. In terms of the LCPT, five optical frequencies become inactive in the Raman spectra which correspond to our results.

3.4. Microstructure distortion

Lattice distortion is defined as a ratio of lattice constant c over a, also called tetragonality, $\delta(a = b, a < c$. δ mainly depends on the mole percent of Ca and not Li). XRD (Fig. 5a and b) was used to identify the crystalline phase of three selected specimens of $Ca_xPb_{1-x}TiO_3$, which is well aligned with the standard tetragonal structure of $PbTiO_3$ (JCPDS No. 6-0452, $a = 3.853 \pm 0.001$ Å, $\alpha = 90^\circ$) [34]. This crystallographic characterization corresponds with the TEM electron diffraction indexing results (Fig. 2c and d). To determine the δ value of the LCPT, the scanning rate of 0.05°/min from diffraction angle at 31–33° for the major spectrum was applied to increase the XRD resolution (Fig. 5b) [34]. The Bragg equation ($d = [(a/h)^2 + (b/k)^2 + (c/l)^2]^{1/2}$) and Scherrer equation ($D = k\lambda/\beta \cos\theta$) were used for calculations of lattice constant and crystallite size, respectively. The δ values for 37 different sensing LCPT elements under various fabrication parameters were determined, of which 11 are shown in Table 2. It was found that three fabrication variables affected the δ value of LCPT the greatest. These were heat-treatment temperature, calcium dopant mole percent and heating rate and they are discussed separately below. XRD directly provides the dimensions of the tetragonality, whereas the Raman spectra yields less active Raman modes (Fig. 4a and b) due to the increase in symmetry of Ca-doped $PbTiO_3$ compared with pure $PbTiO_3$. LCPT tends to be transformed from tetragonal to cubic, which is not observed in this study, confirming our initial purpose of producing tetragonal face-centered structure [41].

3.4.1. Heat-treatment temperature effect on tetragonality

Changes in δ were subject to variation with corresponding changes in temperature. From Table 2, it can be seen that the δ increases from 1.042 → 1.046 → 1.048 when temperature increases from 700 → 800 → 900 °C with a constant mole percent Ca^{2+} at

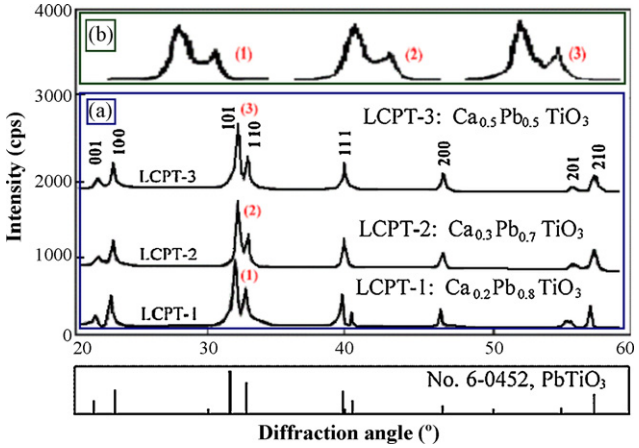

Fig. 5. (a and b) XRD spectra of three selected Li-modified Ca-doped $PbTiO_3$ LCPT sensor, (a) XRD spectra with scanning rate of 2°/min; (b) spectra slow scanning rate of 0.02°/min, (1): the Li-modified $Ca_{0.2}Ti_{0.8}O_3$; (2): Li-modified $Ca_{0.3}Ti_{0.7}O_3$; (3): Li-modified $Ca_{0.5}Ti_{0.5}O_3$.

20 mol%. When heat-treatment temperature increased from 600 to 900 °C (Fig. 6a), the value of δ incrementally increased by 0.54% averagely, which is calculated using this equation:

$$\frac{\delta_{900} - \delta_{600}}{\delta_{900}} \times 100\%$$

where the δ_{900} is the tetragonality of LCPT heated at 900 °C and δ_{600} is the tetragonality at 600 °C. When the heat-treatment temperate surpassed 900 °C, drastic change in δ and crystal growth were noticed. At higher temperatures, the electrons in the d-orbitals of Pb/Ti possessed more kinetics energy, as a result, the elongation along z-axis in the sub-unit of octahedral TiO_6/dodecahedral PbO_{12} was enhanced leading to high lattice distortion (↑δ). In addition, higher temperatures (<900 °C) resulted in crystal growth preferentially along the z-direction. In summary, small nanoparticle size, which are formed at lower temperatures (600 → 900 °C) are desired to decrease crystalline deformation (↓δ) [14].

3.4.2. Ca content effect on tetragonality

It is commonly accepted that $CaTiO_3$ has a cubic structure (lattice constant a, b and c are identical, $\alpha = \beta = \gamma = 90^\circ$) [31], while $PbTiO_3$ has a tetragonal structure (lattice constant c is slight larger than a) [36]. Fig. 6b indicates that the δ value of $PbTiO_3$ is 1.064 and was decreased to 1.040 with increasing Ca mole percent (1–50 mol%). A possible interpretation of this decrease in the δ value was that the Pb^{2+} ions with their larger ionic size were more polarizable than the Ca^{2+} ions. Therefore, the lattice of pure $PbTiO_3$ is readily deformed; leading to a higher δ value. Among 37 specimens, minimal distortion (1.040–1.046) was obtained in samples with Ca (35 mol%) which formed ultra fine powders of particle size ranging from 8 to 30 nm with excellent humidity sensing properties. It can be hypothesized that large specific surface area and appropriate distortion are the most important factors which contribute to high humidity sensitivity.

3.4.3. Heating rate effect on tetragonality

It was determined that δ value of $Ca_{0.35}P_{0.65}TiO_3$ was increased from 1.040 to 1.046 under condition of slow heating rate (2 °C/min). Fig. 6c displayed the tetragonality of other formulations of LCPT ($Ca_{0.10}P_{0.90}TiO_3$, $Ca_{0.15}P_{0.85}TiO_3$, $Ca_{0.20}P_{0.80}TiO_3$, and $Ca_{0.30}P_{0.70}TiO_3$) at three different heating rates (2, 10 and 20 °C/min). The cationic species such as Ca^{2+}, Pb^{2+}, and Ti^{4+} were subject to fast transportation into the molten phase where they

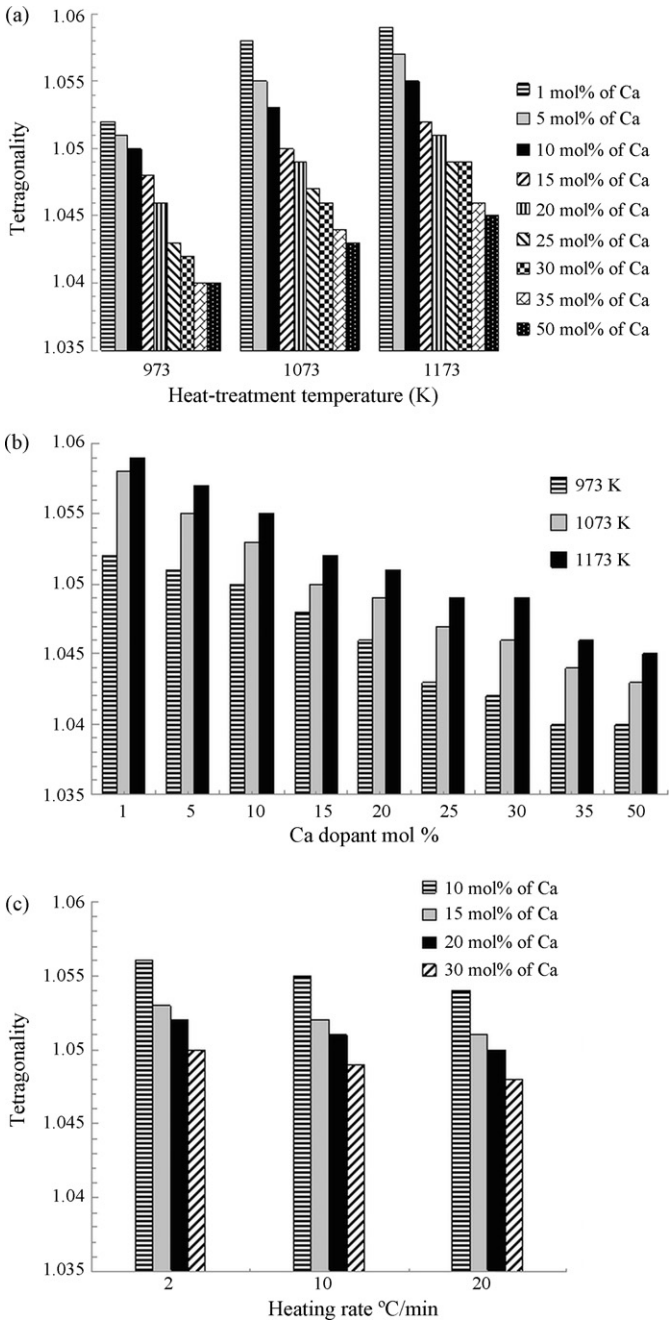

Fig. 6. (a) Tetragonality for LCPT as a function of heating temperature. (b) Tetragonality for LCPT as a function of Ca mole percent. (c) Tetragonality for LCPT as a function of heating rate.

resolidified (Fig. 3b) to form the perovskite structure. This phenomenal resulted in large lattice deformation due to generation of LCPT nanoparticles with large size (Fig. 3b) due to elongated grains whose formation is diffusion-controlled [14]. From our study, rate of heating affected nanoparticle growth, with densification at slower heating rates. This is due to the sol-precursor being rapidly homogenized via large capillary forces present between nano-sized grains (Fig. 3b). Therefore, phase transformation and grain growth can be controlled to synthesize and optimize the required particle size and distribution, respectively.

3.5. Sensor performance

It is hypothesized that when Ca atom substitute for one of the principal Pb atom within the crystal structure of $PbTiO_3$, its electrical properties and structure stability are optimized [52]. Dislocations and point defects in the crystal lattice of $PbTiO_3$ allow shear at lower stress than that needed for a perfect crystal. From our study, it was determined that Ca^{2+} doped $PbTiO_3$ sensor displayed high performance at relative humidity (RH) ≥50% (Fig. 7a1 □ and ○ for Ca-modified and for ● $PbTiO_3$ crystals respectively). This demonstrates that the electrical property and internal stress of the crystal can be enhanced through substitution of Ca for Pb at the A-site. As we mentioned above, Ca^{2+} addition at 0.35 mol% caused the tetragonality of $PbTiO_3$ to decrease from 1.064 to 1.040. The tetragonality decrease eliminated the lattice distortion and anisotropic properties. Therefore, the internal stress was lessened when the sintering temperature was decreased from 900 °C or less to ambient temperature. The addition of Ca^{2+} ions also prevents film cracking and peeling from the Al_2O_3 substrate, which increases sensor mechanical stability. However, the sensor was less sensitive in the low relative humidity range (<50%) due to lack of $\left[V_O^{\bullet\bullet}\right]$ (generated in step (ii) and (iii) *cf.* Section 3.2).

In order to obtain rapid humidity sensitivity over the entire range (RH: 5–95%), alkaline cations ($Na^+/K^+/Li^+$) were added to create $\left[V_O^{\bullet\bullet}\right]$ in Ca-doped $PbTiO_3$ [34]. The addition of Na^+ (○)/K^+ (●) to $Ca_{0.35}Pb_{0.65}TiO_3$ increased sensitivity by three orders of magnitude over the entire humidity range, however, the linearity was non-uniform ($R^2 \sim 0.67$, Fig. 7a2). With addition of Li^+ to $Ca_{0.35}Pb_{0.65}TiO_3$ the sensitivity was also increased with improved linearity ($R^2 \sim 0.99$, Fig. 7a3). This improved response may be attributed to chemisorptions of water molecules on the lattice surface via dipole–dipole interactions due to the high charge density of Li^+ cation. Addition of Li^+ increased the polarization and chemisorptions of water molecules absorbed on the surface (of the LCPT) sensor. Li^+ cation and the negative charged end of oxygen in H_2O molecules formed intermolecular forces (e.g. ion-dipole moments), which enhanced the dissociation of H_2O into proton (H^+) cations and hydroxyl (OH^-) anions (generated in step (i) *cf.* Section 3.2). The protons combined with the lattice oxygen and OH^- anion filled the $\left[V_O^{\bullet\bullet}\right]$ with one electron released as the electricity carrier (generated in step (ii) and (iii) *cf.* Section 3.2). Therefore, electrical current of LCPT sensor increases with corresponding increase in relative humidity. As the relative humidity increases, more water molecules were chemisorbed on the sensor surface. Consequently, more electrons as electricity carrier were released from the lattice, leading to a further increase in measured current, which is directly proportional to the relative humidity. Upon a change in humidity, the hysteresis of the sensor was evaluated to be within ±2% of sensitivity loop with increase in humidity (◊) and decrease in humidity (♦) (Fig. 7b). The small hysteresis effect can be rationalized in terms of water adsorption/desorption. When humidity is increased, water molecules are attracted to the sensor surface through ion-dipole intermolecular force between Li^+ cation and the negative end of the H_2O. During the desorption event, extra energy is required to break this attraction resulting in sensor delay. From our study, it was concluded that the humidity sensing chemical mechanism occurs on the surface of the sensor (Fig. 7c) through two channels (I) protonic conductance due to combination of H^+ with lattice oxygen in the LCPT crystal unit, and (II) occupancy of $\left[V_O^{\bullet\bullet}\right]$ (defect site) by anionic OH^-, releasing charge carriers in the form of electrons (*cf.* Section 3.2).

The sensor response and range were similar or superior to other sensors which utilize piezoelectric micro-cantilever sensing elements via Young's modulus change of their piezoelectric layer [53]. LCPT sensor performance was also comparable to a sensor composed of ceramic nanowires of TiO_2 and organic polymers

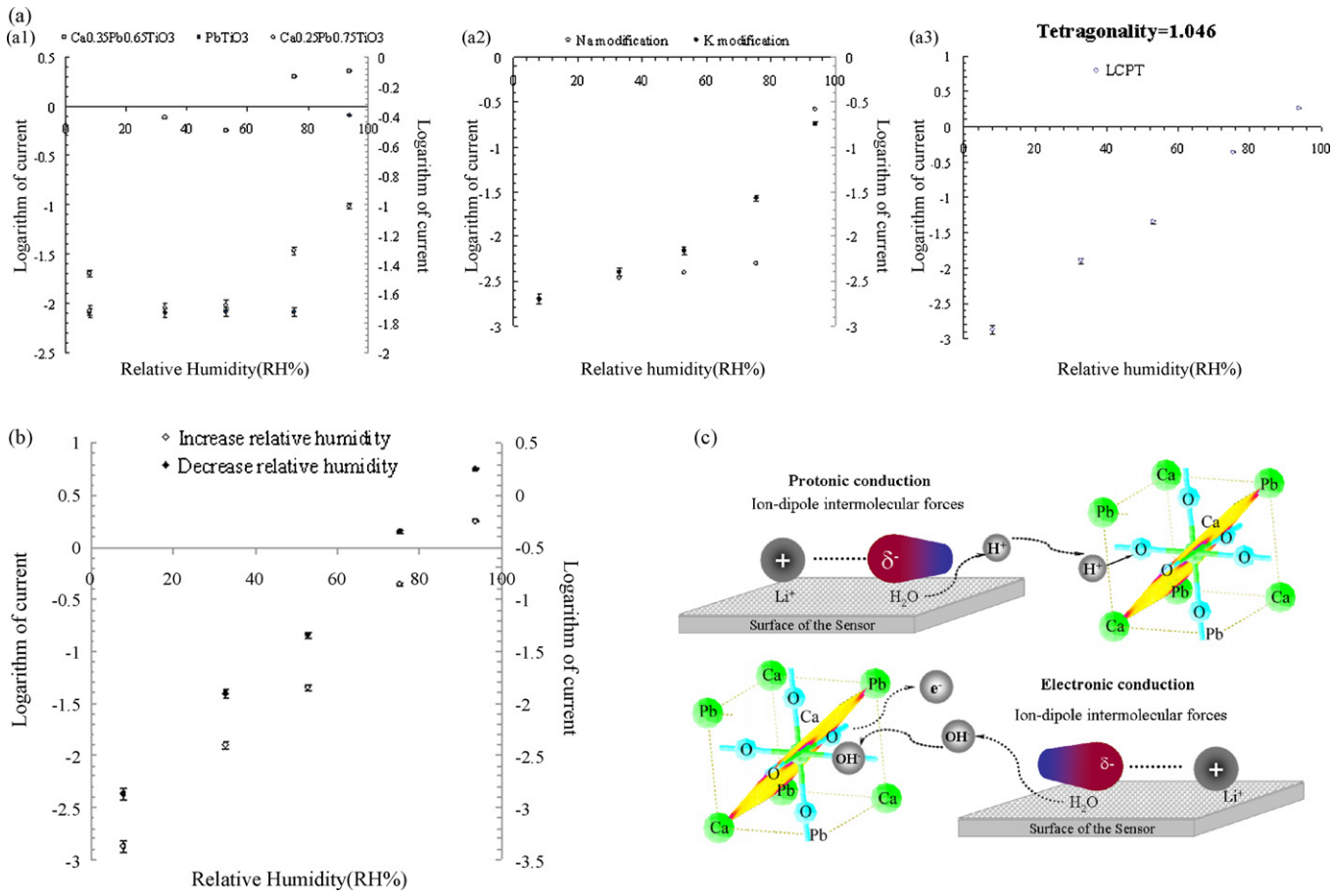

Fig. 7. (a1) Sensitivity of Ca-modified $PbTiO_3$ system; (a2) sensitivity of (Na/K) modified Ca-$PbTiO_3$ nanosensor; (a3) sensitivity of LCPT nanosensor. (b) Hysteresis effect of LCPT during increase and decrease in relative humidity. (c) Chemical mechanisms for humidity detection.

composite films coated on quartz crystal microbalance, although our response time (~11 s at 40% RH) [54] and linearity ($R^2 > 0.99$) were superior with lower hysteresis (±2%) than a silicon based sol sensor [55] with good high temperature stability relative to a single SnO_2 nanowires sensor [56]. The measured recovery time to changes (<1 min 20–95% RH) in humidity was also better than other approaches, such as use of a co-polyaniline nanocomposite thin film sensor [57] with superior long-term stability [58] (tested at 1 week, 4 weeks 12 weeks and 52 weeks, data not shown [34]). The ceramic design affords long-term stability of the sensor matrix.

4. Conclusion

A multi-component humidity sensor was synthesized by the SG method and was composed of tetragonal $PbTiO_3$ crystals. The particle size of the LCPT sensor varied from 8 to 30 nm. The fine particle size resulted in large specific surface area and long phase boundary, which in turn, led to high sensitivity and rapid response time for sensing of humidity. The root mean square of the roughness (along the *z*-axis) was measured to be 54 nm by AFM, which indicated that a large phase boundary was achieved. The humidity sensing mechanisms were due to the formation of ion-dipole intermolecular forces between lithium cation and water molecule, resulting in release of electron as the electricity carrier. Finally, the addition of calcium ions led to a decrease in tetragonality, which in turn improved lattice stability and decreased internal stress of $PbTiO_3$. Cation Li^+ mainly increased water chemisorptions on the surface of the sensor that increased sensor sensitivity across the entire relative humidity range. The operational parameters of the sensor were similar to, or superior to other humidity sensors utilizing nanoparticles, or proteins or organic polymers in their fabrication, in terms of dynamic range, linearity of sensitivity, response time, hysteresis, recovery time, humidity range and long-term stability with the advantage of device portability, ruggedness, ease of fabrication and cost.

Contributors

X. Pan undertook all of the data analysis except the Raman analysis. S. Bashir did the remaining data analysis and generated some of the plots. G. Liang undertook the entire atomic force microscopy characterization component and J. Liu came up with the concept, designed the experimental setup, did all the synthesis, completed the rest of the non-electron microscopy characterization, co-wrote the first draft (with X. Pan and S. Bashir). S. Bashir and J. Liu then re-edited the manuscript and worked on the figures. J. Liu also oversaw the submission process, coordinated the overall workflow and investigations.

Acknowledgements

The authors are grateful to the technical support at Microscope and Imaging Center (MIC) and The Center of Materials Characterization Facility, Texas A&M University (TAMU) to conduct the advanced instrumentation analysis. Dr. Zhiping Luo (at MIC) is acknowledged for his help with TEM electron diffraction indexing. The Research and Development Fund at the College of Arts and Sciences, Texas A&M University-Kingsville is duly acknowledged.

Appendix A. Supplementary data

Supplementary data associated with this article can be found, in the online version, at doi:10.1016/j.talanta.2010.02.063.

References

[1] D.G. Wang, C.Z. Chen, J. Ma, T.H. Liu, Appl. Surf. Sci. 255 (2008) 1637–1645.
[2] M.M. Łencka, R.E. Riman, J. Am. Ceram. Soc. 76 (1993) 2649–2659.
[3] W.L. Li, Q.G. Chi, J.M. Wang, W.D. Fei, J. Non-Cryst. Solids 354 (2008) 5014–5017.
[4] V.G. Bhide, M.S. Hegde, K.G. Deshmukh, J. Am. Ceram. Soc. 51 (1968) 565–568.
[5] Y. Liu, L.H. Ni, G. Xu, C.L. Song, G.R. Han, Y. Zheng, Physica B 403 (2008) 3863–3866.
[6] D. Bao, L. Zhang, X. Yao, J. Mater. Sci. Lett. 18 (1999) 21–23.
[7] W.L. Li, Q.G. Chi, J.M. Wang, W.D. Fei, J. Non-Cryst. Solids. 354 (2008) 5014–5017.
[8] J.B. Liu, Nanostructured $PbTiO_3$-based perovskite thin films used as bifunctional sensor, Ph.D. Thesis, College of Material Science and Engineering, University of Science and Technology Beijing, 2001, pp. 70–85.
[9] S. Kim, M.C. Jun, S.C. Hwang, J. Am. Ceram. Soc. 82 (1999) 289–296.
[10] E. Comini, C. Baratto, G. Faglia, M. Ferroni, A. Vomiero, G. Sberveglieri, Prog. Mater. Sci. 54 (2009) 1–67.
[11] M.G. Lines, J. Alloys Compd. 449 (2008) 242–245.
[12] W.P. Tai, J.G. Kim, J.H. Oh, Y.S. Kim, Sens. Actuators B 105 (2005) 199–203.
[13] G.B. Sergeev, Nanochemistry Moscow, University Book Publishing House, Moscow, 2006 [Chapter 2].
[14] C.J. Brinker, G.W. Scherer, Sol–Gel Science: The Physics and Chemistry of Sol–Gel Processing, Academic Press Inc., New York, 1990, pp. 120–135.
[15] S.M. Selbach, G. Wang, M.A. Einarsrud, T. Grande, J. Am. Ceram. Soc. 90 (2007) 2649–2652.
[16] S.J. Milne, S.H. Pyke, J. Am. Ceram. Soc. 74 (1991) 1407–1410.
[17] N. Tangboriboon, A.M. Jamieson, A. Sirivat, S. Wongkasemjit, Appl. Organomet. Chem. 20 (2006) 886–894.
[18] F. Mitschke, Opt. Lett. 14 (1989) 967–969.
[19] K.K. Kraning, D.A. Sturgeon, Ann. Biomed. Eng. 11 (1983) 131–146.
[20] T. Ohhashi, M. Sakaguchi, T. Tsuda, Physiol. Meas. 19 (1998) 449–461.
[21] Z.M. Qi, I. Honma, H. Zhou, Opt. Lett. 31 (2006) 1854–1856.
[22] K.A. Willets, R.P. Van Duyne, Annu. Rev. Phys. Chem. 58 (2007) 267–297.
[23] R. Bahadur, L.M. Russell, J. Chem. Phys. 129 (2008), 094508–1 to 094508–10.
[24] A. Alshawa, O. Dopfer, C.W. Harmon, S.A. Nizkorodov, J.S. Underwood, J. Phys. Chem. A 113 (2009) 7678–7686.
[25] C. Basavaraja, R. Pierson, D.S. Huh, J. Appl. Polym. Sci. 108 (2008) 1070–1078.
[26] W. Ma, M. Zhang, Z. Lu, Phys. Status Solidi A 166 (1998) 811–815.
[27] A. Liu, Biosens. Bioelectron. 24 (2008) 167–177.
[28] M. Hosokawa, K. Nogi, M. Naito, T.U. Yokoyama, Basic Properties and Measuring Methods of Nanoparticles, Nanoparticle Technology Handbook, Elsevier Science, New York, 2008, pp. 3–48.
[29] I. Szafraniak, M. Połomska, B. Hilczer, Cryst. Res. Technol. 41 (2006) 576–579.
[30] S. Kronholz, S. Rathgeber, S. Karthäuser, H. Kohlstedt, S. Clemens, T. Schneller, Adv. Funct. Mater. 16 (2006) 2346–2354.
[31] G. Burns, B.A. Scott, Phys. Rev. B 7 (1973) 3088–3101.
[32] D. Yu, J.L. Wang, K.R. Zhu, M.S. Zhang, J.M. Hong, Q.R. Gu, Z. Yin, Mater. Lett. 59 (2005) 3272–3275.
[33] J.B. Blum, Mater. Lett. 3 (1985) 360–362.
[34] J.B. Liu, W.C. Li, Y.X. Zhang, Z.M. Wang, Sens. Actuators B 75 (2001) 11–17.
[35] M.M. Kumar, Phys. Status Solidi A 177 (2000) 583–591.
[36] E.R. Leite, E.C. Paris, E. Longo, J.A. Varela, J. Am. Ceram. Soc. 83 (2000) 1539–1541.
[37] K.-S. Chang, B.A. Hernandez, E.R. Fisher, P.K. Dorhout, J. Korean Chem. Soc. 46 (2002) 242–251.
[38] U.V. Waghmare, K.M. Rabe, Phys. Rev. B: Condens. Matter 55 (1997) 6161–6173.
[39] Q.F. Zhow, J.X. Zhang, H.L.W. Chan, C.L. Choy, Ferroelectrics 195 (1997) 211–214.
[40] F. Habbal, E.B. Cargill, (IEEE) Proceedings of the Fourth International Conference on Image Management and Communications, 1996, pp. 75–78, doi:10.1109/IMAC.1995.532564.
[41] Z. Wang, J. Han, J. Liu, Y. Zhang, Acta Chim. Sin. 61 (2003) 1792–1796.
[42] J. Kapusta, P. Daniel, A. Ratuszna, Phase Trans. 72 (2000) 65–181.
[43] X. Meng, Z. Huang, H. Ye, J. Cheng, P. Yang, J. Chu, in: R.E. Jones, R.W. Schwartz, S. Summerfelt, I.K. Yoo (Eds.), Ferroelectric Thin Films, VII, vol. 541, Mater. Res. Soc. Symp. Proc., Warrendale, PA, 1999, p. 723.
[44] S. de Lazaro, E. Longo, J. Ricardo, Surf. Sci. 552 (2004) 149–159.
[45] T. Zhu, G. Han, Z. Ding, Z. Han, J. Mater. Sci. Lett. 15 (1996) 1747–1748.
[46] S. Tinte, K.M. Rabe, D. Vanderbilt, Phys. Rev. B 68 (2003), 144105-1 to 144105-9.
[47] M.A. Zaghete, G.F. Teixeira, G. Gasparotto, J.A. Varela, Multiferroic and Ferroelectric Materials, vol. 1199E, Mater. Res. Soc. Symp. Proc., Boston, MA, 2009, F6.31.
[48] C.B. Yau, Raman, XRD and positron study of ferroelectric films, Ph.D. Thesis, College of Engineering, University of Cincinnati, Cincinnati, 2006, pp. 94–115.
[49] F. Jiang, S. Kojima, Jpn. J. Appl. Phys. 38 (1999) 5128–5132.
[50] A. Rüdiger, R. Waser, J. Alloys Compd. 449 (2008) 2–6.
[51] G.-X. Zhang, Y. Xie, H.-T. Yu, H.-G. Fu, J. Comput. Chem. 30 (2008) 1785–1798.
[52] M. Sharma, H. Sharma, K.K. Raina, J. Phys. Chem. Solids 69 (2008) 2584–2588.
[53] Q. Zhu, W.Y. Shih, W.-H. Shih, Appl. Phys. Lett. 92 (2008), 183505-1 to 183505-3.
[54] P.G. Su, Y.L. Sun, C.C. Lin, Talanta 69 (2006) 946–951.
[55] P.G. Su, C.L. Uen, Talanta 66 (2005) 1247–1253.
[56] Q. Kuang, C. Lao, Z.L. Wang, Z. Xie, L. Zheng, J. Am. Chem. Soc. 129 (2007) 6070–6071.
[57] M.V. Fuke, A. Vijayan, M. Kulkarni, R. Hawaldar, R.C. Aiyer, Talanta 76 (2008) 1035–1040.
[58] F.M. Pontes, E.R. Leite, E. Longo, J.A. Varela, P.S. Pizani, C.E.M. Campos, F. Lanciotti, Adv. Mater. Opt. Electron. 10 (2000) 81–89.